Relation Between Reflection Phase and Surface-Wave Bandgap in Artificial Magnetic Conductors

Mohammadbagher Fereidani Samani, Amir Borji, *Member, IEEE*, and Reza Safian, *Member, IEEE*

***Abstract*—The relationship between the phase of the reflection coefficient and the surface-wave bandgap in planar artificial magnetic conductors (AMCs) is investigated. The periodic surface of the AMC is modeled as a surface impedance and the plane-wave reflection coefficients and the supported surface waves are obtained by this model. Next, the connection between the phase of the reflection coefficient in the fast-wave region and the occurrence of bandgap in the slow-wave region is demonstrated. Theoretical results are verified numerically for two typical AMCs.**

***Index Terms*—Artificial magnetic conductors (AMCs), electromagnetic-bandgap (EBG) structures, periodic surfaces, reflection phase.**

I. Introduction

ARTIFICIAL magnetic conductors (AMCs) are designed to mimic the behavior of perfect magnetic conductors. Therefore, an AMC surface should reflect electromagnetic waves without any phase change in the electric field. A well-known realization of AMC consists of a planar periodic structure printed on a grounded dielectric substrate [1], [2]. This realization is able to exhibit exact in-phase reflection at discrete frequencies that are closely related to the resonances within the periodic surface [1]. The frequency range at which the reflection phase is between $\pm 90^\circ$ (or $\pm 45^\circ$) is often called the in-phase reflection band or AMC bandwidth.

The periodic structure that comprises the AMC could also be engineered to achieve an electromagnetic bandgap (EBG) to suppress surface waves at certain frequency bands. The surface-wave bandgap (SW-BG) of AMCs may overlap with their in-phase reflection band. This property would make the AMC very suitable for antenna applications [1], [2]. A well-known AMC surface that was proposed by Sievenpiper *et al.*, possesses such property [1].

The Sievenpiper's AMC is composed of metallic patches (square or hexagonal) periodically printed on a grounded dielectric slab where each patch has a grounding via. In [3], it was shown that, for a specific set of parameters, the in-phase reflection band of a Sievenpiper's AMC coincides with the SW-BG. However, further research has shown that the SW-BG and the in-phase reflection band are not necessarily correlated in a general Sievenpiper surface [4], [5]. In [6], it has been shown that in Sievenpiper's AMC, the period-to-thickness ratio plays an important role in overlapping of the SW-BG with the in-phase reflection band.

The ambiguous relation between SW-BG and in-phase reflection band has also been investigated in other AMC structures. In [7], an AMC surface is studied that is composed of square-shaped metallic patches with no vias and it is shown that as the period increases, the in-phase reflection band shifts to higher frequencies, while the SW-BG moves to lower frequencies. In [8], a transmission line network model is proposed for periodic patches printed on a grounded slab and a procedure is presented to find the dispersion equation of the surface- and leaky-wave modes from the plane-wave reflection data. The homogenization process used in [8] leads to an equivalent admittance for the periodic surface whose poles and zeros are derived from the reflection data in the fast-wave region. In this paper, we utilize an idea similar to [8]; however, the reflection data is used to develop a surface impedance model that replaces the entire multilayer periodic structure. This model is then used to demonstrate the connection between the phase of reflection coefficient and SW-BG for a general AMC. Despite similarities between this paper and [8], there are notable differences in scope, computational effort, and applicability that will be discussed in Section VI.

This paper is organized as follows. Section II provides the definition of the equivalent surface impedance and the homogenization process of the periodic structure. It also presents the relationship between the surface impedance and the reflection coefficient. In Section III, the analytical form of the dispersion equation is derived using the equivalent surface impedance model. Section IV provides a more in-depth analysis of the dispersion equations for TE and TM modes and the relationship between these equations and the phase of the reflection coefficient is derived. To establish the relationship between the margins of the forbidden band in the slow-wave region and the reflection phase in the fast-wave region, two *bandgap tracking curves* are introduced. On each curve the surface reactance is equal to those on the edges of the bandgap. In Section V, numerical results for two AMC structures, with and without metallic vias, are presented. Both periodic structures have a triangular lattice with hexagonal patches. Finally, Section VI provides the concluding remarks and more discussions on the practical aspects of the method.

II. Reflection From an AMC Surface

Reflection from a uniform planar surface occurs in specular direction and if the state of polarization is preserved after the reflection, properties of the reflected field are described by a scalar

Manuscript received October 16, 2010; revised April 11, 2011; accepted May 13, 2011. Date of publication June 16, 2011; date of current version August 17, 2011.

The authors are with the Department of Electrical and Computer Engineering, Isfahan University of Technology, Isfahan 84156-83111, Iran (e-mail: m.fereidani@ec.iut.ac.ir; amir.borji@gmail.com; rsafian@cc.iut.ac.ir).

Digital Object Identifier 10.1109/TMTT.2011.2157353

reflection coefficient, but if the state of polarization changes after the reflection, a dyadic reflection coefficient must be used to describe the reflected field

$$\bar{\bar{\Gamma}} = \begin{bmatrix} \Gamma_{\mathrm{TE/TE}} & \Gamma_{\mathrm{TE/TM}} \\ \Gamma_{\mathrm{TM/TE}} & \Gamma_{\mathrm{TM/TM}} \end{bmatrix} \tag{1}$$

where $\Gamma_{\mathrm{TE/TM}}$ stands for the ratio of TE reflected electric field to the TM incident electric field and so on.

The reflected field from a planar periodic surface may contain several space harmonics each propagating in a different direction with the main beam always in the specular direction. At a given frequency, if the period is small enough, reflection only occurs in the specular direction and a dyadic reflection coefficient such as (1) can be used to describe the propagating reflected wave. In this section, some important properties of reflection from an AMC surface are highlighted. The AMC surface is then approximated by a uniform, but anisotropic impedance surface and the dyadic reflection coefficient of this surface is derived, which is used to model the reflection from AMC surface under single mode operation.

A. Reflection Properties of an AMC Surface

Let us consider an AMC surface on the x–y plane illuminated by a plane wave given by

$$\varphi^i(x, y, z = 0) = e^{j\boldsymbol{k}_t^i \cdot \boldsymbol{\rho}} \tag{2}$$

where $\boldsymbol{k}_t^i$ is the tangential propagation vector of the incident field and $\rho = x\hat{\boldsymbol{x}} + y\hat{\boldsymbol{y}}$ is the position vector on the x–y plane. Due to the periodic nature of the AMC surface, all Floquet harmonics are excited by the incident field. Hence, any component of the scattered field can be represented by a Floquet expansion [9]

$$\varphi^s(x, y, z) = \sum_{m=-\infty}^{\infty} \sum_{n=-\infty}^{\infty} A_{mn} e^{-j\boldsymbol{k}_t^{mn} \cdot \boldsymbol{\rho}} e^{-jk_{z,mn} z} \tag{3}$$

where A_{mn} and $\boldsymbol{k}_t^{mn}$ are the amplitude and the tangential propagation vector of (m, n)th space harmonic and $k_{z,mn} = \sqrt{k_0^2 - |\boldsymbol{k}_t^{mn}|^2}$. For the general spatial unit cell shown in Fig. 1(a), $\boldsymbol{k}_t^{mn}$ is given by

$$\boldsymbol{k}_t^{mn} = \boldsymbol{k}_t^{00} + m\boldsymbol{k}_1 + n\boldsymbol{k}_2 \tag{4}$$

where $\boldsymbol{k}_t^{00}$ denotes the tangential propagation vector of the $(0, 0)$th Floquet harmonic and $\boldsymbol{k}_1$ and $\boldsymbol{k}_2$ are reciprocal lattice vectors. The reciprocal lattice vectors are obtained from the unit cell vectors of $\boldsymbol{a}_1$ and $\boldsymbol{a}_2$ and satisfy the orthogonality condition $\boldsymbol{k}_i \cdot \boldsymbol{a}_j = 2\pi\delta_{ij}$ (δ_{ij} is the Kronecker delta function) for $i, j = 1, 2$. As a result, $\boldsymbol{k}_i$ is perpendicular to $\boldsymbol{a}_j$ for $i \neq j$ and the magnitude of $\boldsymbol{k}_i$ is determined by

$$k_i = \frac{2\pi}{a_i \sin(\alpha)}, \qquad i = 1, 2 \tag{5}$$

where α is the angle between $\boldsymbol{a}_1$ and $\boldsymbol{a}_2$. In Fig. 1(b), the reciprocal lattice vectors associated with the lattice vectors of Fig. 1(a) are shown.

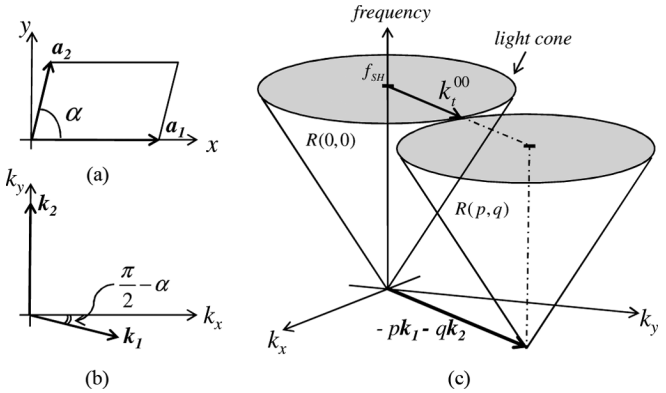

Fig. 1. (a) General unit cell of an AMC surface. (b) Reciprocal lattice vectors of the unit cell in spectral domain. (c) Radiating regions of specular mode, $R(0, 0)$, which is the light cone and the radiating regions of (p, q)th harmonic, $R(p, q)$. At the frequency f_{SH}, $R(0, 0)$ meets $R(p, q)$, which means (p, q)th harmonic becomes radiating.

The total field φ^t is a superposition of the incident field φ^i and the scattered field φ^s ($\varphi^t = \varphi^i + \varphi^s$). Therefore, for one of the Floquet harmonics of φ^s, the tangential propagation vector must be equal to that of the incident field. For simplicity, let $\boldsymbol{k}_t^{00} = \boldsymbol{k}_t^i$, and as a result, the Floquet harmonic of $(m = 0, n = 0)$ is reflected in the specular direction and is called specular harmonic.

For a given AMC surface, if the operating frequency is low enough such that all Floquet harmonics other than the specular one are evanescent and decay exponentially away from the surface, then, as far as the specular harmonic is concerned, the AMC can be replaced by a uniform surface that reproduces the same specular reflection.

Let f_{SH} be the minimum frequency below which all Floquet harmonics, except the specular one, are evanescent in the z direction. To determine this frequency, it is convenient to use the diagram of radiating regions. The so-called radiating region for (p, q)th space harmonic, which is denoted by $R(p, q)$, is basically the light cone shifted by the vector $-p\boldsymbol{k}_1 - q\boldsymbol{k}_2$ in reciprocal space. A typical diagram of radiating regions is shown in Fig. 1(c). For the specular harmonic, $\boldsymbol{k}_t^{00} = \boldsymbol{k}_t^i$, thus $\boldsymbol{k}_t^{00}$ always lies inside the light cone denoted by $R(0, 0)$ in Fig. 1(c) and it is always radiating. When the light cone or $R(0, 0)$ intersects with the nearest radiating region denoted by $R(p, q)$ in Fig. 1(c), the (p, q)th space harmonic becomes radiating. The frequency at which the light cone meets the nearest radiating region is denoted by f_{SH}. Using the geometry of Fig. 1(c), the frequency f_{SH} is readily obtained

$$f_{\mathrm{SH}} = \frac{c}{2\pi} \frac{|-p\boldsymbol{k}_1 - q\boldsymbol{k}_2|}{2} \tag{6}$$

where c is the velocity of light in air. The magnitude of $\boldsymbol{k}_1$ and $\boldsymbol{k}_2$ are calculated using (5) and their angles are shown in Fig. 1(b). Hence, (6) could be written as

$$f_{\mathrm{SH}} = \frac{c}{2} \sqrt{\left(\frac{q}{a_2 \sin\alpha} - \frac{p}{a_1 \tan\alpha} \right)^2 + \left(\frac{p}{a_1} \right)^2} \tag{7}$$

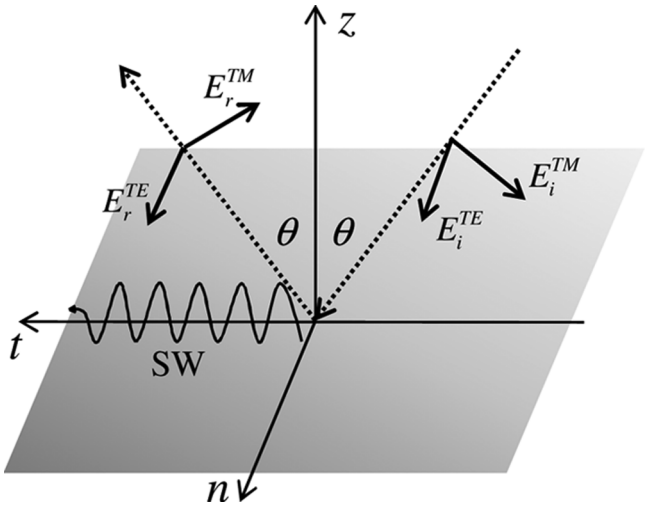

Fig. 2. Surface impedance plane, which models an AMC surface. The incident and reflected plane waves and the surface wave in the t–z plane are shown.

where (p, q) must be chosen to minimize $f_{\rm SH}$ to ensure that for frequencies below $f_{\rm SH}$ all space harmonics, except the specular one, are evanescent.

B. Dyadic Reflection Coefficient

Once the AMC is approximated by a uniform surface, the dyadic reflection coefficient can be determined by the surface impedance concept. In other words, we can replace the AMC surface under single mode operation with an equivalent dyadic surface impedance. Consider the surface of an AMC, as shown in Fig. 2. The surface impedance in k-space is a dyad that relates the tangential components of the magnetic field to those of the electric field at the surface [10]

$$\begin{bmatrix} E_t(k_t,k_n) \\ E_n(k_t,k_n) \end{bmatrix} = \begin{bmatrix} Z_{11}(k_t,k_n) & Z_{12}(k_t,k_n) \\ Z_{21}(k_t,k_n) & Z_{22}(k_t,k_n) \end{bmatrix} \begin{bmatrix} H_t(k_t,k_n) \\ H_n(k_t,k_n) \end{bmatrix} \tag{8}$$

where k_t and k_n are tangential propagation constants along $\hat{t}$ and $\hat{n}$ directions in Fig. 2 and the field components belong to the zeroth-order space harmonic. Note that in Fig. 2, $\hat{t}$ and $\hat{n}$ are not necessarily in the direction of reciprocal lattice vectors. In fact, $\hat{t}$ represents an arbitrary direction within the Brillouin zone, and at the same time, determines the direction of the plane-wave illuminating the structure, i.e., the plane of incidence is the t–z plane. Thus, if $\boldsymbol{k}^i$ is the wave vector of the incident plane wave, then $\hat{n}$ is in the direction of $\hat{z} \times \boldsymbol{k}^i$ and $\hat{t} = \hat{n} \times \hat{z}$.

When the impedance surface in Fig. 2 is illuminated by a time harmonic plane wave, a specular reflection occurs. It was shown in [10] that the tensor of the reflection coefficient is readily determined from the surface impedance tensor $\bar{\bar{\boldsymbol{Z}}}$ using the following expression:

$$\bar{\bar{\boldsymbol{\Gamma}}} = -(C_E + \bar{\bar{\boldsymbol{Z}}} C_H)^{-1}(C_E - \bar{\bar{\boldsymbol{Z}}} C_H) \tag{9}$$

in which

$$C_E = \begin{bmatrix} 0 & \cos\theta \\ 1 & 0 \end{bmatrix} \quad C_H = \frac{1}{\eta_0} \begin{bmatrix} \cos\theta & 0 \\ 0 & -1 \end{bmatrix} \tag{10}$$

where η_0 is the intrinsic impedance of free space and θ is the angle of incidence.

III. Supported Surface Waves by an AMC Surface

In this section, the uniform surface impedance model that was described in Section II is employed to investigate the surface waves supported by the structure. The dispersion equation of surface waves associated with the surface impedance of Fig. 2 is determined by solving source-free Maxwell equations with the boundary condition given in (8). The Maxwell's curl equations in the spectral domain are

$$\begin{vmatrix} \hat{t} & \hat{n} & \hat{z} \\ jk_t & jk_n & jk_z \\ E_t & E_n & E_z \end{vmatrix} = -j\omega\mu_0(H_t\,\hat{t} + H_n\,\hat{n} + H_z\,\hat{z}) \tag{11}$$

$$\begin{vmatrix} \hat{t} & \hat{n} & \hat{z} \\ jk_t & jk_n & jk_z \\ H_t & H_n & H_z \end{vmatrix} = j\omega\epsilon_0(E_t\,\hat{t} + E_n\,\hat{n} + E_z\,\hat{z}) \tag{12}$$

where $|A|$ means the determinant of A. Let us only consider the guided waves along the $\hat{t}$ direction, and as a result, $k_n = 0$ or equivalently $\phi = 0^\circ$. Eliminating the z components in (11) and (12), we obtain the following two linearly independent equations:

$$\begin{bmatrix} E_t(k_t) \\ E_n(k_t) \end{bmatrix} = \begin{bmatrix} 0 & -\eta_0 \dfrac{\sqrt{k_0^2 - k_t^2}}{k_0} \\ \eta_0 \dfrac{k_0}{\sqrt{k_0^2 - k_t^2}} & 0 \end{bmatrix} \begin{bmatrix} H_t(k_t) \\ H_n(k_t) \end{bmatrix} \tag{13}$$

where k_0 is the free-space wavenumber. The set of equations in (13) must be solved using the boundary condition given by (8), which results in the dispersion equation

$$Z_{11}(k_t)Z_{22}(k_t)/{\eta_0}^2 + \Big(\frac{\sqrt{k_0^2 - k_t^2}}{k_0} + \frac{Z_{12}(k_t)}{\eta_0}\Big)\Big(\frac{k_0}{\sqrt{k_0^2 - k_t^2}} - \frac{Z_{21}(k_t)}{\eta_0}\Big) = 0. \tag{14}$$

To obtain the complete dispersion diagram of the AMC surface, one should change the tangential propagation vector $\boldsymbol{k_t} = k_t\hat{t}$ within the irreducible Brillouin zone and find the solution for k_0 in (14). However, in most practical cases, for bandgap determination it is sufficient to move $\boldsymbol{k_t}$ on the edge of the irreducible Brillouin zone.

Since the AMC surface is a periodic structure, its dispersion equation is a periodic function of lateral propagation constant [9]; however, the dispersion equation of the equivalent surface impedance given in (14) does not have this property. When the periodic surface is modeled by a homogeneous surface, the field distribution over the AMC surface is approximated by the dominant Floquet harmonic (or the specular harmonic). This model fails to predict the dispersion behavior inside the bandgaps because a bandgap is a contribution of at least two Floquet harmonics, which form a standing-wave pattern [9]. Hence, the surface impedance model is only able to predict the approximate dispersion behavior outside the bandgap.

IV. Relation Between Reflection Phase and SW-BG in AMC Surfaces

Once the reflection coefficients and dispersion diagram along the $\hat{t}$ direction are obtained, the relation between the reflection phase and SW-BG in AMCs can be investigated.

For simplicity, it is assumed that the reflected wave has the same state of polarization as the incident wave, i.e., the AMC surface creates no cross polarization. Fortunately, most widely used AMC structures cause a very small change in the polarization of incident wave when $\boldsymbol{k}_t^i$ (or $\hat{t}$ in Fig. 2) is parallel to one of the principal lattice vectors. This means $|\Gamma_{\mathrm{TE/TM}}|$ and $|\Gamma_{\mathrm{TM/TE}}|$ are negligible in most cases. From (9), we can find $\bar{\bar{\boldsymbol{Z}}}$ in terms of $\bar{\bar{\boldsymbol{\Gamma}}}$

$$\bar{\bar{Z}} = -C_E(\bar{\bar{\Gamma}} + \bar{\bar{I}})(C_H(\bar{\bar{\Gamma}} - \bar{\bar{I}}))^{-1} \tag{15}$$

where $\bar{\bar{\boldsymbol{I}}}$ is the unit matrix. The diagonal elements of $\bar{\bar{\boldsymbol{Z}}}$ are

$$\begin{aligned} Z_{11} &= A\Gamma_{\mathrm{TM/TE}} \\ Z_{22} &= -A\Gamma_{\mathrm{TE/TM}} \\ A &\triangleq \frac{2\eta_0}{-1-\Gamma_{\mathrm{TE/TE}}-\Gamma_{\mathrm{TM/TM}}+\det(\bar{\bar{\Gamma}})} \end{aligned} \tag{16}$$

which vanish if $\Gamma_{\mathrm{TE/TM}}$ and $\Gamma_{\mathrm{TM/TE}}$ are zero. Furthermore, $Z_{21} = jX_{21}$ and $Z_{12} = jX_{12}$ are purely imaginary for passive and lossless structures [10]. Under these conditions, (9) is reduced to

$$\begin{bmatrix} \Gamma_{\mathrm{TE/TE}} & \Gamma_{\mathrm{TE/TM}} \\ \Gamma_{\mathrm{TM/TE}} & \Gamma_{\mathrm{TM/TM}} \end{bmatrix} = \begin{bmatrix} \dfrac{\frac{jX_{21}}{\eta_0} - \frac{1}{\cos(\theta)}}{\frac{jX_{21}}{\eta_0} + \frac{1}{\cos(\theta)}} & 0 \\ 0 & \dfrac{\frac{jX_{12}}{\eta_0} + \cos(\theta)}{\frac{jX_{12}}{\eta_0} - \cos(\theta)} \end{bmatrix} \tag{17}$$

and (14) results in two separate equations

$$\left(\frac{\sqrt{k_t^2 - k_0^2}}{k_0} + \frac{X_{12}}{\eta_0}\right) = 0 \tag{18}$$

$$\left(\frac{k_0}{\sqrt{k_t^2 - k_0^2}} + \frac{X_{21}}{\eta_0}\right) = 0 \tag{19}$$

where (18) determines the TM polarized surface waves and (19) determines the TE polarized surface waves in the slow-wave region.

The surface reactances $X_{12}(k_t, f)$ and $X_{21}(k_t, f)$ are functions of tangential propagation constant k_t and frequency f. Since the AMC surface is passive and lossless, its surface reactance satisfies the Foster reactance theorem [8]. As a result, X_{12} and X_{21} can be represented by rational functions of frequency with interlaced poles and zeros, therefore, they assume all values from $-\infty$ to $+\infty$ as frequency changes. Furthermore, they can be approximated by rational functions of k_t with no real poles, as was shown in [10].

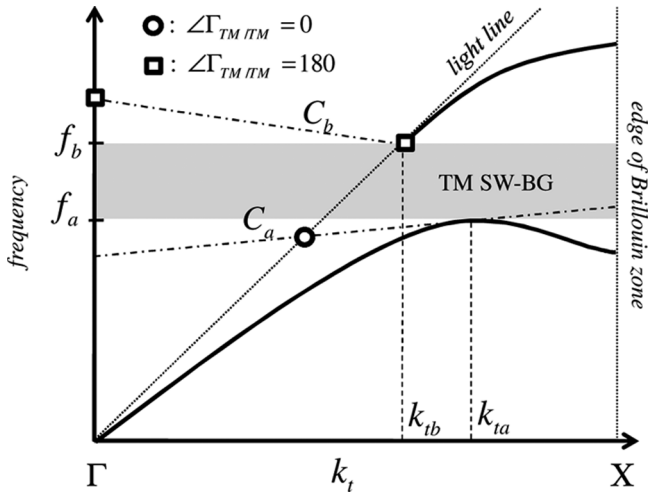

Fig. 3. Typical TM dispersion diagram of an AMC surface. The frequency band (f_a, f_b) is the TM SW-BG. The curves C_a and C_b are the *bandgap tracking curves*. At the point that C_a crosses the light line (indicated by a circle), the reflection phase is always 0°. At all points on the curve C_b in fast-wave region the reflection phase is always 180°.

Using (17), one can calculate $\Gamma_{\mathrm{TE/TE}}$ and $\Gamma_{\mathrm{TM/TM}}$ as a function of incident angle θ, or equivalently, as a function of tangential propagation constant $k_t = k_0 \sin(\theta)$ in the fast-wave region where the value of k_t varies from 0 at normal incidence ($\theta = 0°$) to k_0 at grazing incidence ($\theta = 90°$). In other words, the behavior of the surface impedance for fast waves ($k_t < k_0$) is determined by the reflection characteristics of the structure. However, in (18) and (19), the behavior of the surface impedance for slow waves ($k_t > k_0$) is needed to obtain the supported surface waves. This is achieved by analytic continuation of the surface reactance functions into the slow-wave region [8].

A. TM Case

Consider the dispersion diagram of a typical EBG surface for TM surface waves, as shown in Fig. 3. A surface-wave mode emerges from the light line at frequency f_b, while the diagram for the lowest order mode reaches its maximum at frequency f_a somewhere in the slow-wave region. The frequency band between f_a and f_b is an SW-BG. This behavior is typical in the so-called mushroom-type structures (patches with vias), but is not usually observed in uniplanar EBGs. A thorough review of published data reveals, however, that the dispersion curves of most conventional EBG/AMC/PBG structures typically show a maximum at the corner of Brillouin zone (at point X or M) and the minimum point always occurs on the light line. The peak has also been observed between points M and Γ for some multilayer uniplanar structures. In mushroom-type structures, however, the peak of the dispersion curve of the fundamental mode occurs between Γ and X corners of the Brillouin zone after which the mode becomes a backward wave or left handed [11]. A similar peak also occurs between Γ and M points. Even for these structures the dispersion curves of higher order modes show the typical maxima at X or M points. In any case, the location of this

peak (k_{ta}) does not change anything in the method presented here. Let X_{12}^i denote the value of surface reactance at frequency f_i ($i = a$ or b) on the two edges of the bandgap, then according to (18), we can write

$$X_{12}^i = X_{12}(k_{ti}, f_i) = \frac{-\eta_0\sqrt{k_{ti}^2 - k_{0i}^2}}{k_{0i}} \tag{20}$$

where $k_{0i} = 2\pi f_i\sqrt{\mu_0\epsilon_0}$ and k_{ti} is the tangential propagation constant of the supported surface wave at frequency f_i. Let C_i ($i = a, b$) denote the locus of the points on the k_t–f plane (for $0 < k_t < k_{ti}$) where the surface reactance $X_{12}(k_t, f)$ equals X_{12}^i. We call C_i a *bandgap tracking curve*. Analytic properties of surface reactance function, which were mentioned before, ensure that C_i is an analytic curve in the k_t–f plane. These two curves are shown in Fig. 3. The idea is to find these two curves by just a few simulations of the reflection coefficient of the structure under plane-wave illumination. Extrapolation of these curves into the slow-wave region would provide us information on the SW-BG. The phase of reflection coefficient for all points located on the two bandgap tracking curves can be obtained from (17) when $X_{12}(k_t, f) = X_{12}^i$

$$\angle\Gamma_{\mathrm{TM/TM}} = 180^\circ + 2\arctan\left(\frac{X_{12}^i}{\eta_0\cos(\theta)}\right). \tag{21}$$

The points (k_{ti}, f_i) at the two extreme edges of the bandgap (in the slow-wave region) and the points where the reflection phase is given by (21) (within the fast-wave region) lie on the same bandgap tracking curve C_i. From (20), it can be concluded that $X_{12}^a = -\eta_0\sqrt{k_{ta}^2 - k_{0a}^2}/k_{0a} < 0$ and $X_{12}^b = 0$. Therefore, at all points on C_a, the surface reactance is a constant negative value and at the point C_a crosses the light line ($\theta = 90^\circ$), there is in-phase reflection ($\angle\Gamma_{\mathrm{TM/TM}} = 0^\circ$). At all points on C_b, in the fast-wave region, the surface reactance is zero and $\angle\Gamma_{\mathrm{TM/TM}} = 180^\circ$.

B. TE Case

For the TE case, the typical dispersion diagram shown in Fig. 4 is considered. The "typical" behavior was explained in Section IV-A. The frequency band of (f_b, f_a) is the passband of TE surface waves. Hence, outside this frequency band is the TE bandgap. From (19), the top and bottom edges of the TE bandgap denoted by (k_{ti}, f_i) ($i = b, a$) are solutions of the following equation:

$$X_{21}^i = X_{21}(k_{ti}, f_i) = \frac{-\eta_0 k_{0i}}{\sqrt{k_{ti}^2 - k_{0i}^2}}. \tag{22}$$

The phase of the reflection coefficient for all the points at which $X_{21}(k_t, f) = X_{21}^i$ is obtained from (17),

$$\angle\Gamma_{\mathrm{TE/TE}} = -180^\circ - 2\arctan\left(\frac{X_{21}^i}{\eta_0}\cos(\theta)\right). \tag{23}$$

Similar to the TM case, there is an analytic bandgap tracking curve denoted by C_i in Fig. 4 that passes through the edge of surface-wave passband at (k_{ti}, f_i) in the slow-wave region and the reflection phase on this curve is given by (23) in the fast-wave region. Furthermore, from (22), it can be concluded that

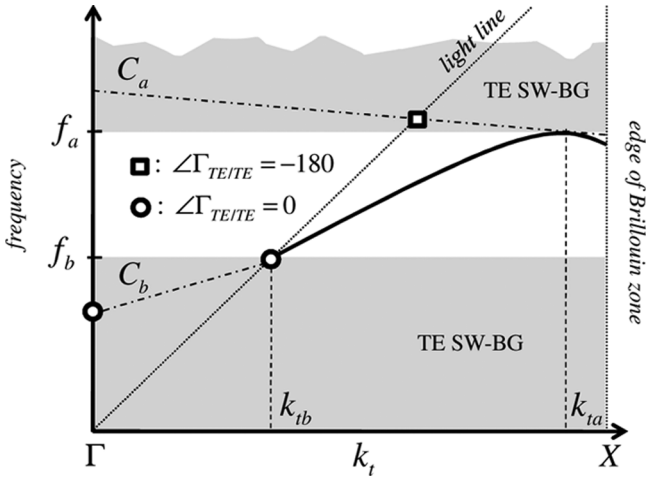

Fig. 4. Typical TE dispersion diagram of an AMC surface. The frequency band outside of (f_b, f_a) is TE bandgap. The curves C_a and C_b are the *bandgap tracking curves*. At the point that C_a crosses the light line (indicated by a square symbol), the reflection phase is always -180°. On the curve C_b in the fast-wave region, the reflection phase is always 0°.

$X_{21}^a = -\eta_0 k_{0a}/\sqrt{k_{ta}^2 - k_{0a}^2} < 0$ and $X_{21}^b = -\infty$. As a result, at all points on C_a, the surface reactance is a constant negative value and at the point C_a crosses the light line ($\theta = 90^\circ$), the reflection phase is -180°. On the other hand, C_b, in the fast-wave region, is the locus of all points where $\angle\Gamma_{\mathrm{TE/TE}}$ is 0°.

C. Determination of Bandgap Tracking Curves

For conventional AMC structures, which are usually made of metallic patches printed on grounded dielectric substrates with or without grounding vias, the procedure for determination of bandgap tracking curves can be summarized as follows.

1) The point (f_a, k_{ta}) is determined by carrying out dispersion analysis of the periodic structure within the frequency range of $0 < f < f_{\mathrm{SH}}$ along the edges of the irreducible Brillouin zone. Following the discussion on the typical location of k_{ta} in EBG structures (see Section IV-A), the dispersion analysis is only needed on one edge of the Brillouin zone. Only a few points of the dispersion diagram of the lowest order mode are required to find (f_a, k_{ta}).
2) The value of surface reactance at point (f_a, k_{ta}) is determined using (20) for TM mode or (22) for TE mode.
3) A few points of each bandgap tracking curve (C_a and C_b) in a visible or fast-wave region must be determined using plane-wave reflection analysis. To find these curves, the phase of the reflection coefficient for a number of plane waves within the same frequency range $0 < f < f_{\mathrm{SH}}$ and for a few angles of incidence between $\theta = 0$ and $\theta < 90^\circ$ are calculated using full-wave numerical simulations. For the TM mode, those points for which the phase of reflection is 180° and those for which the reflection phase is given by (21) are extracted from the above data set. These two sets of points lie on C_b and C_a curves, respectively. The process for the TE mode is similar, except that the reflection phase of 0° and (23) must be used.

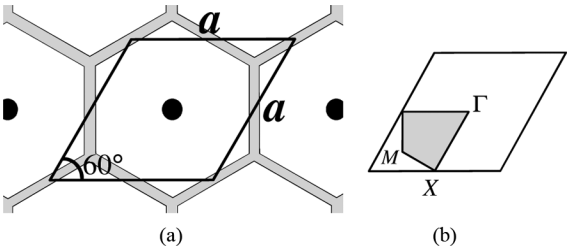

Fig. 5. (a) AMC surface proposed by Sievenpiper *et al.* [1] is composed of hexagonal metallic patches in a triangular lattice. The unit cell of this surface is the rhombus with $a = 2.4$ mm. The separation between the hexagonal patches is 0.15 mm and each patch is connected to the ground plane with a metallic via of 0.36-mm diameter. The dielectric substrate with $\epsilon_r = 2.2$ and thickness of 1.6 mm was considered. (b) Shaded area shows the irreducible Brillouin zone.

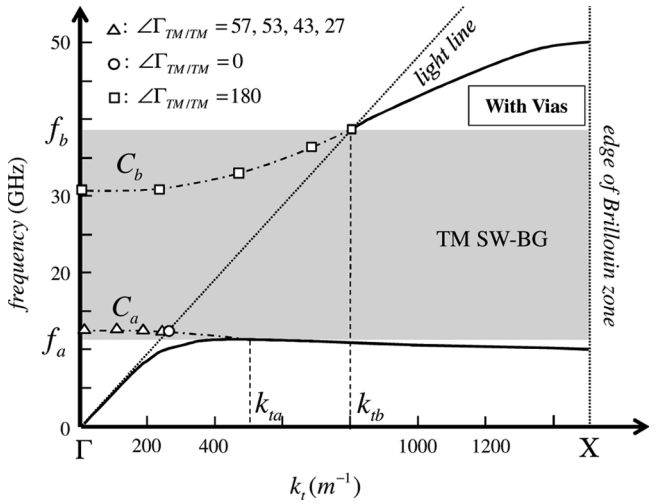

Fig. 6. Dispersion diagram of TM surface waves in $\Gamma - X$ direction and the bandgap tracking curves for the AMC surface in Fig. 5. The points at which the reflection phase is given by (21) are indicated by triangles ($\angle\Gamma_{\mathrm{TM/TM}} = 57°, 53°, 43°, 27°$). Small squares and circle represent points with reflection phase of 180° and 0°, respectively.

4) A polynomial curve-fitting procedure is applied to the discrete points obtained in 3) in order to obtain an approximate analytic form of the bandgap tracking curves in the k_t–f plane.

V. Numerical Verification

In this section, the predicted relations between the reflection phase and SW-BG are examined for two well-known AMC surfaces. The first example is the surface that was proposed by Sievenpiper *et al.* in [1]. The geometry and physical parameters of this AMC surface are shown in Fig. 5(a). The second example is the same structure when the grounding vias are removed. The surface impedance model and our predictions are valid up to the frequency f_{SH}. From (7), f_{SH} that is associated with the unit cell geometry in Fig. 5 is $f_{\mathrm{SH}} = 72.16$ GHz. In the first case, the point k_{ta} occurs between the points Γ and X on the edge of the Brillouin zone, while in the second example, it occurs at point X. Therefore, for both structures, the relationship was investigated on the $\Gamma - X$ edge of the Brillouin zone that is shown in Fig. 5(b). A full-wave analysis was performed for five angles of plane-wave incidence ($\theta = 0°, 21.25°, 42.5°, 63.75°, 85°$) along with a frequency sweep at each incident angle.

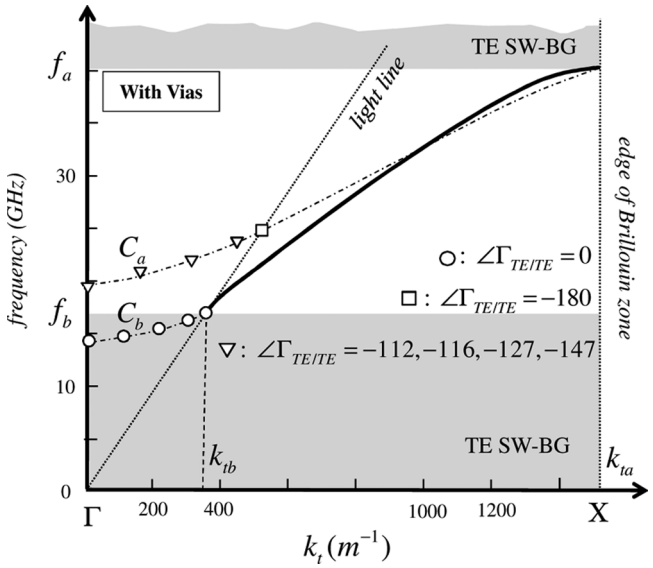

Fig. 7. Dispersion diagram of TE surface waves in $\Gamma - X$ direction and the bandgap tracking curves for the AMC surface in Fig. 5. The points at which the reflection phase is given by (23) are indicated by triangles ($\angle\Gamma_{\mathrm{TE/TE}} = -112°, -116°, -127°, -147°$). Small square and circles represent points with reflection phase of $-180°$ and 0°, respectively.

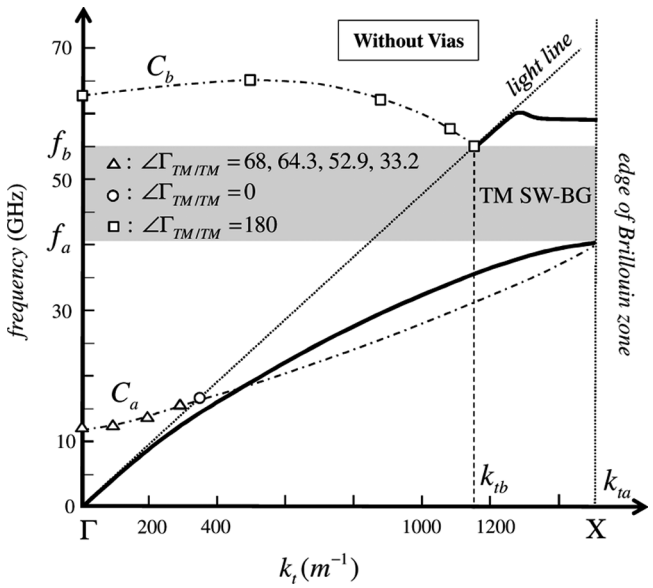

Fig. 8. Dispersion diagram of TM surface waves and the bandgap tracking curves for the structure in Fig. 5 when the vias are removed. The points at which the reflection phase is given by (21) are indicated by triangles ($\angle\Gamma_{\mathrm{TM/TM}} = 68°, 64.3°, 52.9°, 33.2°$). Small squares and circle represent points with reflection phase of 180° and 0°, respectively.

The results for TM and TE waves in the first example are presented in Figs. 6 and 7, respectively. For the TM case, second-order polynomials were used for interpolation and extrapolation of bandgap tracking curves. For the TE case, third-order polynomials were employed. One may have to use higher order polynomials for structures with high angular instability where the reflection phase changes rapidly with the angle of incidence. To improve the accuracy when extrapolating C_a inside the slow-wave region, the point (f_a, k_{ta}) is included in the polynomial curve-fitting procedure. When the vias are removed, the results for TM and TE waves are shown in Figs. 8 and 9, respectively.

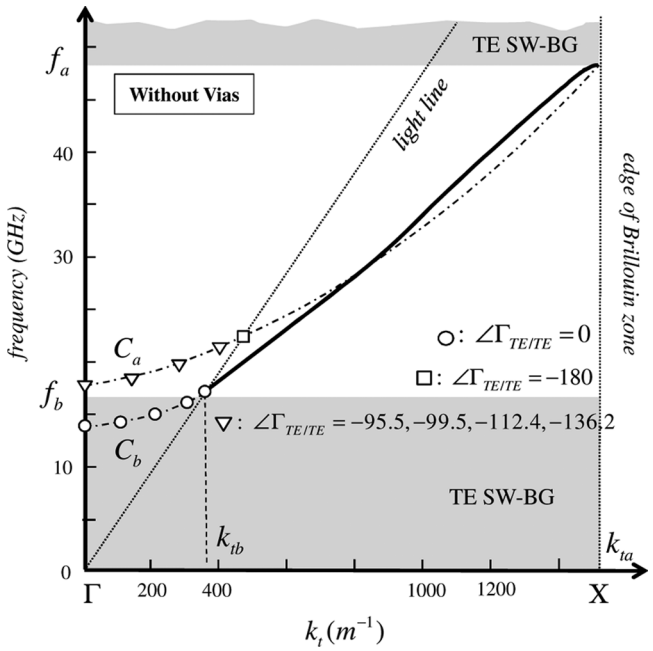

Fig. 9. Dispersion diagram of TE surface waves and the bandgap tracking curves for the structure in Fig. 5 when the vias are removed. The points at which the reflection phase is given by (23) are indicated by triangles ($\angle\Gamma_{\mathrm{TE/TE}} = -95.5°, -99.5°, -112.4°, -136.2°$). Small square and circles represent points with reflection phase of $-180°$ and $0°$, respectively.

In this case, second-order polynomials were used for curve fitting.

Above results show that, for TE modes, removing the vias only shifts the second bandgap towards higher frequencies, but the shape of bandgap tracking curves (especially C_b), and thus, the angular behavior of the structure remain relatively unchanged. However, for TM modes, removing the vias has a significant effect on the bandgap tracking curves and the dispersion diagram. A prominent change is that the backward wave in Fig. 6 is disappeared in Fig. 8.

VI. Concluding Remarks

The relationship between the reflection phase and SW-BG in AMCs was investigated. This connection was established by introducing two *bandgap tracking curves* in the k_t–f plane. These curves connect the two margins of the SW-BG to the points with certain reflection phase in the fast-wave region while the surface reactance remains constant on each curve. A polynomial curve fitting was employed to obtain the approximate analytic form of the bandgap tracking curves using only a few data points gathered from numerical simulations.

As mentioned at the beginning of this paper, there are notable differences between the method presented here and that of [8]. First, the method presented in [8] was developed to calculate the complete dispersion diagram of a frequency-selective surface (FSS) structure (both for surface waves and leaky waves) from the phase of reflection coefficient. However, our aim here is to establish a relationship between the two margins of the SW-BG in the slow-wave region and the phase of reflection coefficient in the fast-wave region and to gain some insight as to how they change with respect to each other. Secondly, since the method presented in [8] tries to calculate the complete dispersion diagram and also because of the type of modeling that was used (a rigorous admittance model for the FSS), the method requires a huge amount of computational effort. This includes the extraction of the poles and zeros of the FSS admittance from the reflection data, as well as the rotation of the admittance matrix at each frequency with angle α, which must be determined numerically [8]. Although this method could eventually give us the information that we are seeking in this paper, it is computationally too excessive for our purpose. We do not need to find the whole dispersion diagram, and with the type of modeling that we use, the approach presented here is computationally more efficient. Finally, the most prominent difference between the proposed method and that of [8] is the use of a surface impedance model for the FSS instead of the transmission line network model; in other words, our proposed homogenization process is different. Basically, when looking from the top, any multilayer periodic structure can be replaced by a uniform surface impedance as long as the frequency is below the single harmonic frequency, as explained in Section II. Therefore, unlike the method presented in [8], the proposed technique can be equally applied to EBG structures with or without metallic vias or even to PBG structures where a dielectric layer contains periodic inclusions.

A key property in finding the relation between reflection phase and bandgap is the angular stability of the AMC surface, which affects the way the reflection phase changes by the angle of incidence. The angular stability heavily influences the shape of the bandgap tracking curves. Studying several types of EBG structures (including printed dipoles and rectangular and hexagonal patches with and without vias) showed that as we move toward more angularly stable structures, the curve C_b, which is the locus of the points with a constant reflection phase, tends to become a horizontal straight line in the k_t–f plane. Similarly, the curve C_a also tends toward a horizonal line with less variations of the reflection phase on it.

The relation between reflection phase and SW-BG can be utilized to develop an effective methodology for designing AMC surfaces in antenna applications where it is much more useful if the AMC and EBG frequency bands overlap so that the effects of surface waves are reduced. The technique presented here provides a quick way to predict whether these two bands overlap. This is due to the fact that in structures with high angular stability, one can obtain an estimate of where the bandgap occurs without resorting to cumbersome dispersion analysis in the slow-wave region, which is much more costly and time consuming than simple plane-wave reflection analysis. For TM modes, it was observed that at the cross point between the curve C_a and the light line, the phase of reflection was always $0°$. If we just obtain the locus of the points for which the reflection phase is $0°$ and $180°$ and find their cross points with the light line, then, in an angularly stable structure, we have a very good estimate of the bandgap without the need to do any dispersion analysis. In other words, in such cases, we do not need to generate the actual bandgap tracking curve C_a. Similarly, in the case of TE modes, it was observed that at the cross point between the curve C_a and the light line the phase of reflection was always $-180°$. If we just obtain the locus of the points for which the reflection phase is $0°$ and $-180°$ and find their cross

points with the light line, then we have a very good estimate of the bandgap if the structure is angularly stable. This means we do not need to generate the actual bandgap tracking curve C_a. Such plane-wave reflection simulations are very fast and we only need to do them for a few angles of incidence and then use the interpolation scheme to generate the curves and extrapolate their cross points with the light line.

In this paper, it was assumed that the reflected wave from the AMC surface had the same state of polarization as the incident wave, i.e., the cross polarization was negligible. Although in most AMC surfaces this assumption is valid, it is not true in general and efforts are under way to extend the method for the general case.

REFERENCES

[1] D. Sievenpiper, L. Zhang, R. F. J. Broas, N. G. Alexopolous, and E. Yablonovitch, "High-impedance electromagnetic surfaces with a forbidden frequency band," *IEEE Trans. Microw. Theory Tech.*, vol. 47, no. 11, pp. 2059–2074, Nov. 1999.

[2] Z. Li and Y. Rahmat-Samii, "PBG, PMC and PEC ground planes: A case study of dipole antennas," in *Proc. IEEE AP-S Int. Symp.*, Jul. 16–21, 2000, vol. 2, pp. 674–677.

[3] F. Yang and Y. Rahmat-Samii, "Reflection phase characterization of an electromagnetic bandgap (EBG) surface," in *Proc. IEEE AP-S Int. Symp.*, Jun. 16–21, 2002, vol. 3, pp. 744–747.

[4] A. Aminian, F. Yang, and Y. Rahmat-Samii, "In-phase reflection and EM wave suppression characteristics of electromagnetic bandgap ground planes," in *Proc. IEEE AP-S Int. Symp.*, Jun. 22–27, 2003, vol. 4, pp. 430–433.

[5] S. Clavijo, R. E. Diaz, and W. E. McKinzie, "Design methodology for Sievenpiper high-impedance surfaces: An artificial magnetic conductor for positive gain electrically small antennas," *IEEE Trans. Antennas Propag.*, vol. 51, no. 10, pp. 2678–2690, Oct. 2003.

[6] L. Li, Q. Chen, Q. Yuan, C. Liang, and K. Sawaya, "Surface-wave suppression bandgap and plane-wave reflection phase band of mushroom-like photonic bandgap structures," *J. Appl. Phys.*, vol. 103, no. 2, Jan. 2008, Art. ID 023513.

[7] G. Goussetis, A. P. Feresidis, and J. C. Vardaxoglou, "Tailoring the AMC and EBG characteristics of periodic metallic arrays printed on grounded dielectric substrate," *IEEE Trans. Antennas Propag.*, vol. 54, no. 1, pp. 82–89, Jan. 2006.

[8] S. Maci, M. Caiazzo, A. Cucini, and M. Casaletti, "A pole-zero matching method for EBG surfaces composed of a dipole FSS printed on a grounded dielectric slab," *IEEE Trans. Antennas Propag.*, vol. 53, no. 1, pp. 70–81, Jan. 2005.

[9] R. E. Collin and F. J. Zucker, *Antenna Theory. Part 2*. New York: McGraw-Hill, 1968.

[10] D. J. Hoppe and Y. Rahmat-Samii, *Impedance Boundary Conditions In Electromagnetics*. Boca Raton, FL: CRC, 1995.

[11] A. Sanada, C. Caloz, and T. Itoh, "Planar distributed structures with negative refractive index," *IEEE Trans. Microw. Theory Tech.*, vol. 52, no. 4, pp. 1252–1263, Apr. 2004.

Mohammadbagher Fereidani Samani was born in Isfahan, Iran, in 1984. He received the B.S. and M.S. degrees in electrical engineering from the Isfahan University of Technology, Isfahan, Iran, in 2007 and 2010, respectively.

He is currently with the Electrical and Computer Engineering Research Center, Isfahan University of Technology. His research activities are focused on artificial impedance surfaces and their applications, FSSs, and EBG structures.

Amir Borji (S'99–M'04) was born in Tehran, Iran, in August 1971. He received the B.Sc and M.Sc degrees in electrical engineering from the Isfahan University of Technology, Isfahan, Iran, in 1994 and 1998, respectively, and the Ph.D degree in electrical engineering from the University of Waterloo, Waterloo, ON, Canada, in 2004.

From 2004 to 2006, he was with the Department of Electrical and Computer Engineering, University of Waterloo, as a Post-Doctoral Fellow, where he conducted research on compact millimeter-wave microstrip and slot array antennas, millimeter-wave leaky wave antennas, and numerical analysis of planar periodic structures. In September 2006, he joined the Department of Electrical and Computer Engineering, Isfahan University of Technology, as an Assistant Professor, where he has also been the Director of the Communications Engineering Group since 2009. His research interests include synthesis, design, and optimization of multiple coupled resonator filters, theory and applications of multilayer periodic structures such as EBGs, AMCs, FSSs and photonic bangaps (PBGs), leaky-wave antennas, and guided-wave optics.

Reza Safian (S'04–M'09) received the B.Sc. degree in electrical engineering from the Isfahan University of Technology, Isfahan, Iran, in 1999, the M.A.Sc. degree in electrical engineering from from McMaster University, Hamilton, ON, Canada, in 2003, and the Ph.D. degree in electrical engineering from the University of Toronto, Toronto, ON, Canada, in 2008.

From 1999 to 2002, he was an RF Design Engineer with the Electrical and Computer Engineering Research Center (ECERC), Isfahan University of Technology. In 2008, he joined the faculty of the Isfahan University of Technology, where he is currently an Assistant Professor with the Electrical and Computer Engineering Department. His technical interests include basic electromagnetic theory, microwave circuits, wave propagation in dispersive materials, and microwave imaging.